

www.acsnano.org

Tuning Morphologies and Reactivities of Hybrid Organic—Inorganic Nanoparticles

Joanna Schneider, Jason X. Liu, Victoria E. Lee, Robert K. Prud'homme, Sujit S. Datta, and Rodney D. Priestley*



Cite This: ACS Nano 2022, 16, 16133-16142



ACCESS I

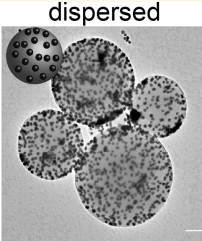
Metrics & More

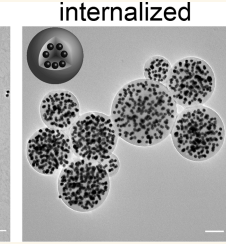


s Supporting Information

ABSTRACT: Hybrid nanoparticles (hNPs), or nanoparticles composed of both organic and inorganic components, hold promise for diverse energy and environmental applications due to their ability to stabilize reactive nanomaterials against aggregation, enhancing their ability to pervade tortuous spaces and travel long distances to degrade contaminants in situ. Past studies have investigated the use of polymer or surfactant coatings to stabilize nanomaterials against aggregation. However, fabrication of these materials often requires multiple steps







and lacks specificity in the control of their morphologies and reactivities. Here, we demonstrated a method of producing stable hNPs with tunable morphologies by incubating polystyrene nanoparticles formed via Flash NanoPrecipitation with citrate-stabilized gold nanocatalysts. Using this simple fabrication technique, we found that gold adsorption to polystyrene nanoparticles was enabled by the presence of a good solvent for polystyrene. Furthermore, changing process parameters, such as gold incubation time, and molecular parameters, such as polymer molecular weight and end-group functionality, provided control over the resultant nanocatalyst loading and dispersal atop hNPs. We classified these morphologies into three distinct regimes—aggregated, dispersed, or internalized—and we showed that the emergence of these regimes has key implications for controlling reaction rates in applications such as heterogeneous catalysis or groundwater remediation. Specifically, we found that hNPs with gold nanocatalysts embedded *below* the surfaces of polystyrene nanoparticles exhibited slower bulk catalytic reduction capacity than their disperse, surface-decorated counterparts. Taken together, our work demonstrates a simple way by which hNPs can be fabricated and presents a method to control catalytic reactions using reactive nanomaterials.

KEYWORDS: hybrid nanoparticle, nanocatalyst, adsorption, aggregation, dispersal, internalization

The development of hybrid materials, or materials containing both organic and inorganic components, is of significant interest for applications ranging from drug delivery and bioimaging 1-5 to heterogeneous catalysis. 6-9 Hybrid materials are of particular interest in groundwater remediation, where subsurface injection of nanomaterials is a promising technique due to the capacity of these materials to travel long distances, pervade small spaces, and degrade contaminants via a number of in situ chemical reactions. 1 However, most widely used nanomaterials, such as zero valent iron nanoparticles (nZVI) and metal oxides, aggregate over time scales on the order of minutes, reducing their reactivity and mobility in tortuous, confined pore spaces. 14-16 Others, like gold (Au) nanoparticles, are too expensive for widespread use due to the large amounts of material that need to be injected, thus preventing their widespread implementation.¹⁷

Most research on the use of reactive nanoparticles has focused on their stabilization through the use of surfactants or polymer coatings. However, there is currently limited work that addresses a method to both stabilize reactive

nanoparticles and control the rate at which they degrade contaminants, which is of critical importance in environmental remediation. Hybrid nanoparticles (hNPs) may provide a solution to this problem due to their ability to stabilize and control the loading of reactive nanomaterials. Several methods have been explored to produce nanostructured colloids; in particular, methods such as self-assembly, 23-25 self-organized precipitation (SORP), 26-29 and Flash NanoPrecipitation (FNP) have been explored to produce phase separated polymeric nanoparticles. Furthermore, the capabilities of some of these methods have been expanded to produce hybrid nanoparticles that contain both an organic polymeric

Received: May 10, 2022 Accepted: October 6, 2022 Published: October 12, 2022





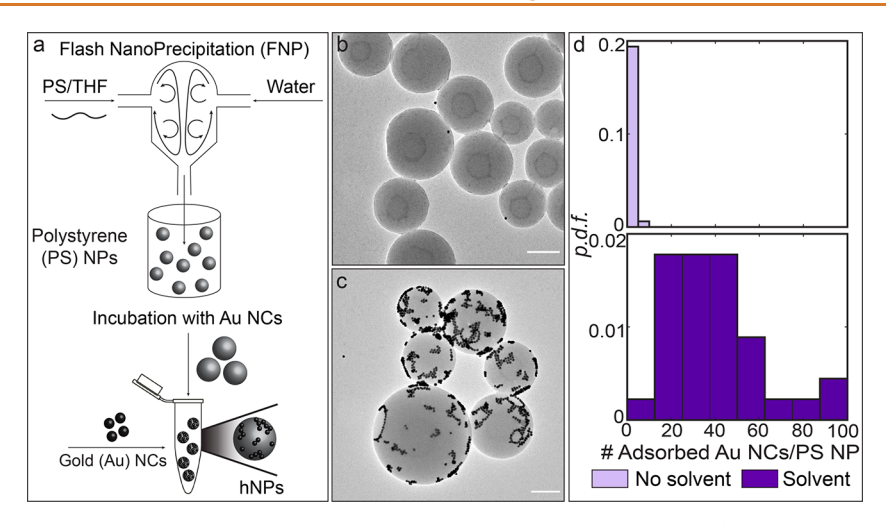


Figure 1. Presence of a good solvent for PS during incubation with Au NCs promotes adsorption. (a) Schematic of hNP formation via Flash NanoPrecipitation (FNP) and incubation with Au NCs. PS NPs are represented schematically and in transmission electron microscopy (TEM) images in gray, and Au NCs are represented in black. (b) Hybrid NP formation in the absence of a good solvent. When THF is removed prior to incubation of PS NPs with Au NCs, there is no appreciable adsorption of Au NCs to PS NPs. (c) Hybrid NP formation in the presence of a good solvent. When THF is present in the PS NP and Au NC mixture during incubation, Au NCs adsorb to PS NPs. (d) Comparison of the probability density function (p.d.f.) of adsorbed Au NCs per PS NP in the absence (top) or presence (bottom) of a good solvent. All PS NPs have <10 Au NCs adsorbed to their surfaces when THF is absent during incubation. When THF is present, most PS NPs have >10 Au NCs adsorbed to their surfaces. Scale bars in (b) and (c) are 200 nm.

component and an inorganic metal component. While widespread use of some of these methods may be hindered by more complex, multistep fabrication techniques, ^{33–36} self-assembly, ^{37,38} encapsulation in nanoshells or nanopores, ³⁹ and self-organized precipitation (SORP) ^{40–42} hold promise due to their ability to precisely place inorganic components on or within an organic component.

In particular, SORP presents a promising method for hNP production because it harnesses equilibrium phase separation to specifically confine metal nanoparticle placement within polymeric nanoparticles. In several studies, gold nanoparticles were stabilized using polymers so they could be readily incorporated into block copolymer solutions in the presence of a poor solvent, resulting in localization of gold nanoparticles in the same domain as its polymer stabilizer. 40-42 In some examples, gold nanoparticles were internalized in lamellae or localized atop polymer nanoparticles.²⁸ However, despite the success of this method in producing hybrid nanostructured particles, previously reported experimental methods require modification of the metal component to be compatible with the appropriate polymeric domain and require several days to produce the final particle suspensions, presenting opportunities for improvement in total production time, and simplified, scalable fabrication.

To overcome these limitations, we have demonstrated a simple, two-step fabrication technique that employs Flash NanoPrecipitation to scalably produce hNPs with tunable morphologies. In this study, we showed that the good solvent present in the polymer nanoparticle suspension from FNP could be utilized to improve the mobility of inorganic metal nanocatalysts atop these polymer nanoparticles, thus enabling the formation of hNPs. We demonstrated that the resultant nanocatalyst loading and dispersion atop polymeric nanoparticles can be tuned through changes to molecular parameters (i.e., polymer molecular weight, polymer end-group functionality, and nanocatalyst size) or process parameters (i.e., incubation time). By analyzing the size and number of "clusters" formed by individual metal nanocatalysts

atop polymeric nanoparticles, we revealed that diffusion of gold nanocatalysts (Au NCs) on their surfaces was hindered by increasing polymer molecular weight, and therefore viscosity due to polymer chain dynamics, resulting in aggregation of metal nanocatalysts atop hNPs. However, the addition of charged polymer end-groups provided stronger electrostatic interactions that hindered diffusion and gave rise to hNPs with disperse metal nanocatalyst decoration in which metal nanocatalysts became embedded within polymeric nanoparticles. We also found that this internalization of metal nanocatalysts within polymeric nanoparticles was strongly correlated with lower bulk reaction rates of a model reduction reaction when compared to surface-decorated morphologies. Overall, our work reveals a simple method to fabricate hNPs with tunable metal nanocatalyst dispersal and loading, which controls their ability to tune catalytic reaction rates, and may have important implications for catalytic reduction of contaminants that permeate groundwater aquifers.

RESULTS AND DISCUSSION

Adsorption Due to the Presence of a Good Solvent.

To produce hNPs, we mixed polystyrene nanoparticles (PS NPs) produced via FNP with previously fabricated gold nanocatalysts, as shown in Figure 1a. Before incubation with Au NCs, we first removed tetrahydrofuran (THF) from the PS NP suspension via rotary evaporation because the presence of a toxic, volatile organic solvent in the final particle suspension is undesirable for many applications, such as environmental remediation and drug delivery. All However, we observed that Au NCs incubated with PS NPs in 100% water resulted in little to no Au NC adsorption (Figure 1b). When we quantified this observation for many transmission electron microscopy (TEM) images, we observed that most PS NPs adsorbed fewer than 5 Au NCs when THF was not present during the incubation step (Figure 1d, top). Furthermore, the few Au NCs that were attached appeared to be caught between PS

ACS Nano www.acsnano.org Article

NPs while drying on TEM grids, rather than becoming embedded atop their surfaces.

However, when residual THF from PS NP fabrication was not removed prior to incubation with Au NCs, we observed a striking difference. In a final solvent mixture of 22.2% THF and 78.8% water, Au NCs strongly adsorbed atop PS NPs despite the fact that there were no known attractive functional groups on PS NP surfaces to stabilize citrate-coated Au NCs. In one example, we observed the formation of two-dimensional (2D) Au NC aggregates atop PS NPs (Figure 1c). Furthermore, across varying surface configurations of Au NCs atop PS NPs, we found that most PS NPs contained between 10 and 60 Au NCs adsorbed to their surfaces, representing considerable adsorption, which we define as number of adsorbed Au NCs per PS NP > 10 (Figure 1d, bottom). These results demonstrate that the presence of THF is necessary to facilitate Au NC adsorption to PS NPs.

To address the presence of THF in the final hNP suspension, we also investigated the impact of post-incubation rotary evaporation. By completing the incubation step in the previously employed solvent mixture of 22.2% THF and 78.8% water before removing THF, we found that Au NC adsorption atop PS NPs obtained through incubation in the presence of THF was retained once THF was removed (SI Figure 1). Moreover, the number of adsorbed Au NCs per PS NP remained above the threshold for considerable adsorption (i.e., >10 Au NCs) under these conditions.

To probe the sensitivity of Au NC adsorption atop PS NPs to THF concentration, we next investigated the ability of hNPs to form by adding Au NCs of varying diameter (5, 20, and 40 nm) to PS NP suspensions with varying solvent compositions. First, we considered the control case in which Au NCs were incubated with PS NPs without THF (Figure 2(a-c)i). For all Au NC sizes, we anticipated that no adsorption would occur, which is indeed what we observe in the first column of Figure 2. In all samples without THF, we observed a few Au NCs, but the number of adsorbed Au NCs per PS NP \ll 10. Furthermore, TEM images revealed that most Au NCs still present after centrifugation appeared to be aggregated between PS NPs rather than adsorbed atop them, which we hypothesized to be a result of drying on TEM grids.

When we increased the THF concentration to 10%, we began to observe differences in Au NC adsorption across the tested range of Au NC sizes (Figure 2(a-c)ii). Specifically, we observed hNP formation when $d_{Au} = 5$ nm (Figure 2a.ii), while incubation with 10% THF was insufficient to result in considerable adsorption of 20 or 40 nm Au NCs atop PS NPs (Figure 2b.ii, c.ii). This difference in adsorption suggests that THF may enhance the mobility of Au NCs within PS. Ten percent THF was enough to enhance Au NC mobility within a surface layer ≥ 5 nm thick because we see hNP formation with 5 nm Au NCs, but that layer must also be thinner than 20 nm because we did not see hNP formation with Au NCs \geq 20 nm (Figure 2b.ii, c.ii).

Increasing the THF concentration further to 20% revealed a similar trend (Figure 2(a-c)iii). Here, we observed that 20% THF was sufficient to produce hNPs in the presence of both 5 and 20 nm Au NCs, suggesting that the surface layer of PS allowed for enhanced mobility within an outer radius of \geq 20 nm (Figure 2a.iii, b.iii). We also began to see a change in 40 nm Au NC adsorption (Figure 2c.iii), but the average number of adsorbed Au NCs remained below the threshold for considerable adsorption of >10 Au NCs per PS NP (SI Figure

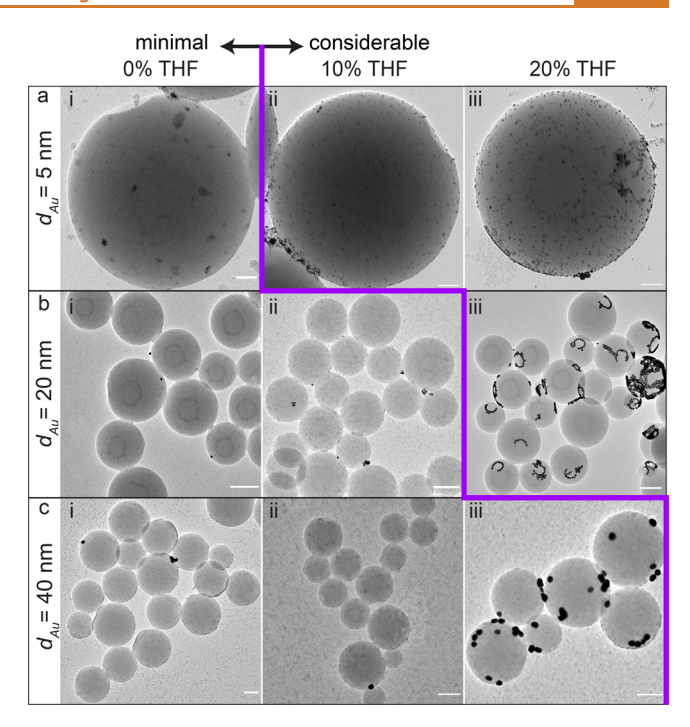


Figure 2. THF concentration impacts the ability of Au NCs to adsorb atop PS NPs. (a) Adsorption of 5 nm Au NCs occurred only when a minimum concentration of 10% THF was present during incubation. (b) Adsorption of 20 nm Au NCs occurred when 20% THF was present during incubation. (c) We observed slight adsorption of 40 nm Au NCs to PS NPs at a THF incubation concentration of 20%, but appreciable adsorption occurred at a threshold value of 30% THF. The purple line delineates the THF concentration above which the transition between minimal (<10 Au NCs) and considerable (>10 Au NCs) adsorption occurred. Scale bars in (a) are 50 nm. Scale bars in (b) and (c) are 200 nm.

2). We believe this transition was more gradual because Au NCs were at most 2 times larger than the PS NP surface layer, potentially allowing for some favorable adsorption (Figure 2c.iii). Despite this more gradual adsorption onset, we only began to see considerable adsorption of 40 nm Au NCs at higher THF concentrations, ≥30% (SI Figure 2). Thus, the strong correlation between increasing THF concentration and the ability for larger Au NCs to adsorb atop PS NPs establishes a criterion for their formation, as indicated by the purple stair-step that delineates the transition between minimal and considerable adsorption of Au NCs atop PS NPs (Figure 2).

Surface Aggregation of Au NCs Due to Diffusion. We next harnessed the versatility of our two-step fabrication process to alter hNP surface decoration by exploring one process parameter, incubation time, and one molecular parameter, PS molecular weight. First, we investigated how incubation time of PS NPs with excess Au NCs affected the surface decoration of hNPs, for which we use a final solvent mixture of 22.2% THF and 78.8% water. Using PS with $M_{\rm n}$ = 100 kg/mol as our baseline, we observed disperse Au NCs on the surfaces of PS NPs (Figure 3a) after 1 h. We consider Au NCs to be disperse when a large population of Au NC clusters contains fewer than 2 Au NCs and none or few Au NC clusters exceed sizes of 10 Au NCs. For example, after 1 h of incubation, >40% of clusters contained fewer than 2 Au NCs, and >90% of clusters contained fewer than 10 Au NCs (Figure 3d).

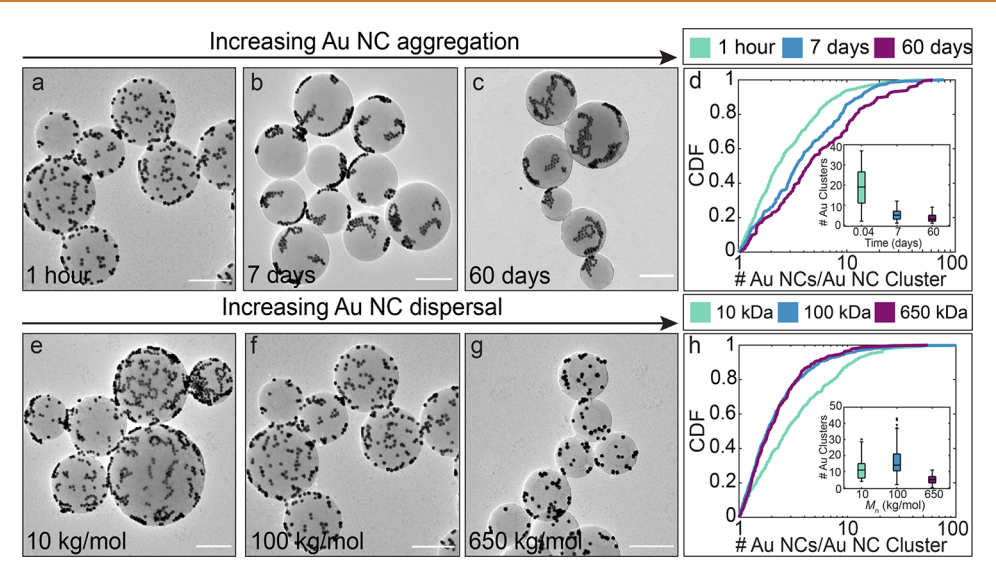


Figure 3. Diffusion time scale of PS chains impacts Au NC dispersal. Hybrid nanoparticles fabricated with 100 kg/mol PS and incubated with Au NCs for (a) 1 h, (b) 7 days, and (c) 60 days reveal a transition from disperse to aggregated surface decoration. (d) Cumulative distribution function (CDF) of Au NC cluster sizes over time. The CDF indicates a shift from smaller to larger cluster sizes as time increases. Inset shows a box and whisker plot of the number of clusters per PS particle over time. As the size of clusters increases, the number of clusters decreases. (e) hNPs fabricated with 10 kg/mol PS, (f) 100 kg/mol PS, and (g) 650 kg/mol PS at a constant incubation time of 1 h indicate increasing dispersal due to longer diffusion time scales as molecular weight increases. (h) CDF of Au NC cluster sizes with varying molecular weight indicates that hNPs with low molecular weight PS exhibit greater surface aggregation. Inset shows a box and whisker plot of the number of clusters per PS particle with varying molecular weight. All scale bars are 200 nm.

However, longer incubation times with excess Au NCs did not result in greater adsorption, but rather, there was greater Au NC aggregation atop PS NPs. Increasing incubation time from 1 h to 7 days caused a 15% reduction in the population of clusters ≤ 2 Au NCs. This observation indicates that at intermediate incubation times between 1 and 7 days, Au NCs began to diffuse across the surfaces of PS NPs, aggregating to increase the population of intermediate-sized clusters (Figure 3b). As incubation time was increased another order of magnitude to 60 days, we observed the presence of even larger clusters (Figure 3c). Between 1 h and 60 days, the population of large clusters increased by over 20% (Figure 3d), while the average number of Au NCs adsorbed per PS NP for long incubation times remained constant (SI Figure 3), suggesting that by the 60-day point, aggregation occurred via coalescence of larger clusters, rather than by the motion of individual Au NCs.

This shift toward larger clusters as incubation time increased is further supported by quantification of the number of Au NC clusters on each PS NP. The inset of Figure 3d shows a decrease in the median number of clusters per PS NP from 19 clusters after 1 h of incubation, to 5 clusters after 7 days, and 3 clusters after 60 days. We hypothesized that the initial stark decrease in the number of clusters between 1 h and 7 days occurred due to diffusion of numerous small clusters. However, once aggregates became larger, their diffusive motion became sluggish. While they were still able to coalesce into larger aggregates, the rate of such fusion events was reduced drastically due to both the longer diffusion times necessitated by the larger average cluster size as well as the more limited number of possible interactions due to the presence of fewer clusters.

The strong dependence of both Au NC cluster size and total number of Au NC clusters on incubation time suggests that Brownian diffusion of Au NCs was strongly influenced by the viscosity of PS NPs. To further probe this hypothesis, we

altered the resultant PS NP viscosity by varying the PS molecular weight employed in the FNP solvent stream. We fabricated PS NPs using each molecular weight ($M_n = 10$, 100, and 650 kg/mol) and incubated them with Au NCs for 1 h. PS NPs fabricated from 10 kg/mol PS exhibited strong aggregation, in which Au NCs formed 2D worm- and ringlike structures on PS NP surfaces (Figure 3e). However, as molecular weight increased, formation of large aggregates on PS NP surfaces was suppressed, giving rise to disperse surface decoration of Au NCs on PS NP surfaces (Figure 3f,g). We again quantified aggregation via an analysis of Au NC cluster sizes (Figure 3h). When we assessed the cumulative distribution function (CDF) of Au NC clusters on the surfaces of 10, 100, and 650 kg/mol PS NPs, we found that hNPs fabricated with 10 kg/mol PS exhibited 20% more Au NC clusters >2 Au NCs in size than their higher M_n counterparts, consistent with our observations.

Finally, to describe the transition from aggregated to disperse surface decoration that we observed with increasing molecular weight, we used a simple scaling argument to compare the viscosities of the PS NPs themselves by approximating each nanoparticle as a polymer melt. Despite our hypothesis that residual THF penetrates some distance into PS NPs, 45 we make this approximation because the polymer chains within PS NPs are collapsed into dense aggregates during FNP, with polymer volume fractions, x, of at least 0.58 in the precipitated 10 kg/mol PS NPs, much less than its respective overlap concentration, reported as a volume fraction, x^* of approximately 0.02. 46,47 For PS with a molecular weight below the entanglement molecular weight ($M_e = 17 \text{ kg/}$ mol) the viscosity scales as $\eta_{PS} \sim N$, where N is the number of monomers within the polymer chain. For PS with a molecular weight that exceeds $M_{\rm e}$, $\eta_{\rm PS} \sim N^3/N_{\rm e}^2$, where $N_{\rm e} = M_{\rm e}/m_0$ and m_0 is the molecular weight of the PS monomer. 48 Thus, we

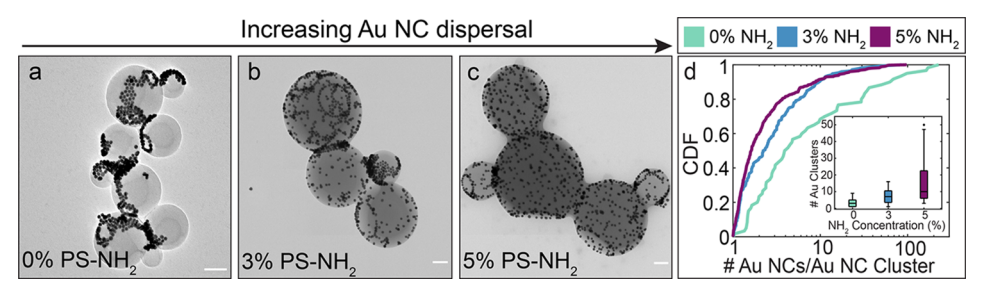


Figure 4. Low PS-NH₂ concentrations promote Au NC dispersal. Hybrid NPs fabricated with (a) 0%, (b) 3%, and (c) 5% 10 kg/mol PS-NH₂ reveal enhanced dispersal as PS-NH₂ content increases. (d) CDF of Au NC cluster sizes reveals a trend toward more disperse Au NCs on the surfaces of PS NPs with increasing NH₂ content. Inset shows that the number of clusters per PS NP increases concomitantly. All scale bars are 100 nm.

found that $\eta_{100\text{kDa}}/\eta_{10\text{kDa}} \sim O(100)$, while $\eta_{650\text{kDa}}/\eta_{10\text{kDa}} \sim O(10^5)$.

This scaling provides a rationale for the Au NC aggregation observed in Figure 3. For example, following the viscosity ratio $\eta_{100\text{kDa}}/\eta_{10\text{kDa}}$, we would expect Au NCs to become aggregated atop 100 kg/mol PS at time scales 100X longer than 10 kg/mol PS. Indeed, when we compared the morphology of 100 kg/mol hNPs at incubation times 100X longer than 10 kg/mol hNPs, we saw similar extents of aggregation when we compared Figure 3b and Figure 3e. Furthermore, following the viscosity ratio, $\eta_{650\text{kDa}}/\eta_{10\text{kDa}}$, we would not expect to see comparable morphologies to 10 kg/mol hNPs until time scales $O(10^5 \text{ hours})$ longer (SI Figure 4).

While this scaling argument helped to link qualitative similarities in Au NC configurations atop PS NPs obtained by either changing molecular weight or incubation time, we still observed a difference in the trends between the number of Au NC clusters observed per PS NP over time versus molecular weight (insets to Figure 3d,h). When we varied PS molecular weight, the number of clusters per PS NP increased between 10 kg/mol and 100 kg/mol, consistent with the inset to Figure 3d, but we saw a sudden decrease in the number of clusters per PS NP at 650 kg/mol (inset to Figure 3h). We attributed this discrepancy to our experimental method, in which we held the inlet mass of PS during FNP constant and the volume ratio of PS NPs to Au NCs constant during incubation. Using a constant inlet mass of PS does not necessarily correspond to constant PS NP size, particularly at higher M_n . The smaller PS NP size obtained from 650 kg/mol PS ($d = 113 \text{ nm} \pm 11 \text{ nm}$) versus those obtained from 10 kg/mol ($d = 302 \text{ nm } \pm 17 \text{ nm}$) or 100 kg/mol ($d = 300 \text{ nm} \pm 12 \text{ nm}$) implies that a greater number of small PS NPs were incubated with Au NCs. Thus, the PS NP surface area to Au NC mass ratio increased due to the increased surface area of 650 kg/mol PS NPs, and a smaller number of Au NCs adsorbed to each PS NP as a result.

Dispersal and Internalization of Au NCs atop and within PS NPs. Despite the lack of attractive interactions between PS and citrate-stabilized Au NCs, we observed the formation of hNPs whose surface decoration characteristics were sensitive to diffusion. We hypothesized that by adding amine-terminated polystyrene (PS–NH₂) to the FNP solvent stream, stronger interactions between the positive end-groups of PS–NH₂ and negatively charged citrate-stabilized Au NCs would hinder diffusive motion of Au NCs, promoting the presence of more disperse Au NCs atop PS NPs.

We employed PS with a molecular weight M_n = 10 kg/mol to assess the effect of electrostatic interactions on Au NC

mobility atop PS NPs. Typically, complete aggregation occurred on hNPs made from PS with $M_{\rm n}=10~{\rm kg/mol}$ within a 24-h incubation period (SI Figure 5), so we analyzed Au NC dispersal for a range of PS–NH $_2$ concentrations after 24 h of incubation to assess the ability of electrostatic interactions to stabilize disperse Au NCs atop PS NPs. For comparison, we show the hNP morphology produced from 10 kg/mol PS (0% PS–NH $_2$) after 24 h of incubation with Au NCs (Figure 4a), which exhibited almost complete aggregation, or the formation of a single, large Au aggregate per PS particle (Figure 4d and inset).

By varying PS-NH₂ concentrations from 0% to 50%, we detected two distinct morphological regimes that arise due to the presence of charged end groups, which we term "dispersal" (Figure 4) and "internalization" (Figure 5). We first explore the "dispersal" regime, within which we see the suppression of Au NC aggregation on the surfaces of PS NPs. When PS NPs were fabricated from 3 vol % PS-NH₂, we still saw ring-like aggregates similar to those that we saw in the absence of PS-NH₂ (Figure 4b), but we also began to see a much larger presence of disperse, single Au NCs, as indicated by the difference between the CDFs for 0% PS-NH2 and 3% PS-NH₂ (Figure 4d). As the concentration of PS-NH₂ increased to 5%, we observed a 45% increase in the population of Au NC clusters <2 Au NCs and a concomitant 20% decrease in the population of Au NC clusters >10 Au NCs, indicating that Au NCs shifted toward nearly complete surface dispersal (Figure

The approach to complete dispersal at 5% PS-NH₂ is also supported by our analysis of the total number of clusters per PS NP. Here, we saw that the distribution in the number of clusters became much wider at 5% PS-NH₂ than it was at 3% PS-NH₂ (inset to Figure 4d). This stark difference in number of clusters per PS particle supports our observation that the diffusive process that formed midsized worm- and ring-like structures gave rise to smaller Au NC aggregates or single Au NCs. This nuance is further supported by the shift in the CDFs of 3% and 5% PS-NH₂ morphologies. While the entire distribution shifted toward smaller clusters between 0% and 3% PS-NH₂, between 3% and 5%, the majority of this shift occurred only in the population of midsize clusters because worm- and ring-like structures began to disappear.

When the PS-NH₂ volume percentage was increased to 10%, we observed that Au NCs began to embed themselves beneath the surfaces of PS NPs in a process we term "internalization" (Figure 5a). While Au NCs were just beneath the surfaces of PS NPs at 10% PS-NH₂, for PS-NH₂ concentrations greater than 10%, Au NPs were immersed

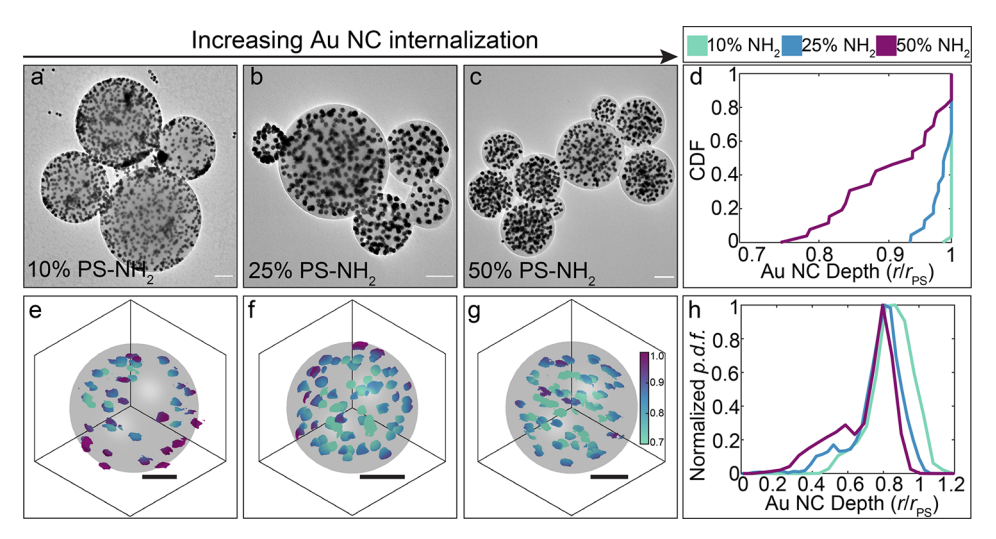


Figure 5. Au NCs become internalized above a threshold concentration of PS-NH₂. Hybrid NPs fabricated from 10 kg/mol PS with (a) 10%, (b) 25%, and (c) 50% 10 kg/mol PS-NH₂ reveal increasing degrees of internalization as PS-NH₂ content increases. (d) CDF of Au NC depth within PS NPs obtained from 2D images reveals that as PS-NH₂ content increases above 10%, Au NCs penetrate deeper into PS NPs. Three-dimensional (3D) tomographic reconstructions of Au NC locations within PS NPs containing (e) 10%, (f) 25%, and (g) 50% PS-NH₂ content shows increasing depth of internalization as PS-NH₂ content increases. The color scale corresponds to the depth within the PS NP that Au NCs are located, normalized to the radius of the PS NP. (h) Normalized radial density distribution plot of Au NCs within PS NPs. As PS-NH₂ content increases, the peak density shifts toward further internalization and a population of internalized Au NCs develops. Scale bars in (a-c) are 100 nm. Scale bars in (e-g) are 50 nm.

completely. Previous work using a two-polymer blend in the FNP process shows that when the interfacial tension, $\gamma_{\rm polymer1-water} < \gamma_{\rm polymer2-water}$, the resulting colloids exhibit a core—shell morphology in water. 30 Thus, because PS–NH $_2$ is more hydrophilic than PS ($\gamma_{\rm PS-NH}_2$ -water $<\gamma_{\rm PS-water}$), it should form a core—shell structure with PS–NH $_2$ as the shell.

However, when PS/PS-NH₂ NPs are incubated with citrate-stabilized Au NCs, we must also consider the charge neutralization effects that occur when NH₃⁺ and COO⁻ groups interact. We can explore the impact of the interactions between NH₃⁺ and COO⁻ groups by quantifying the charge ratio, or the molar ratio of NH₃⁺ to COO⁻ groups present during incubation. For example, the surfaces of hybrid NPs made with 10% PS-NH₂ became saturated with Au NCs because the charge ratio was $\ll 1$ (Figure 5a). As a result, we expected that all Au/PS-NH₂ complexes were free to exist at or close to the surface because there was NH₃⁺ in excess of COO⁻. Our 2D analysis of TEM images confirmed this expectation (Figure 5d), and also suggests that the Au/PS-NH₂ complex was still less hydrophobic than PS.

As PS-NH₂ content increased, the shell it formed became thicker and the NH₃⁺ to COO⁻ charge ratio eventually exceeded 1, at a calculated crossover concentration of approximately 21% (Supplementary Calculations). Above 21% PS-NH₂, we began to see internalization of Au NCs (Figure 5b, c). When the charge ratio eventually exceeded 1, there was free PS-NH₂ available to exist at the surface of hNPs, which we hypothesize is energetically favorable because $\gamma_{\rm PS-water} > \gamma_{\rm PS-NH_2/Au-water} > \gamma_{\rm PS-NH_2-water}$, and can be seen clearly by the presence of an Au NC-free ring on the outside of 50% PS-NH₂ NPs (Figure 5c). Because the charge ratio was ≫1 in this case, compatibilization of Au NCs within PS via hydrophobic ion pairing enabled their miscibility and is therefore also energetically favorable. 49,50 Thus, both enhanced surface wetting and miscibility acted as energetic driving forces in the formation of these internalized hNPs. Our observations

were further supported by the CDF of Au NC depth within PS, which showed that >80% of hybrid NPs fabricated with 50% PS-NH₂ contained only internalized Au NCs (Figure 5d).

Having quantified Au NC internalization from two-dimensional (2D) images, we also performed TEM tomography to confirm the three-dimensional (3D) structure of the hNPs. TEM images of three isolated hNPs containing 10%, 25%, and 50% PS-NH $_2$ were acquired at tilts ranging from -60° to $+60^{\circ}$. Three-dimensional tomographic reconstructions from these tilted images mapped the spatial distribution of Au NCs within these hNPs (Figure 5e-g), showing good qualitative agreement with the Au NC placement estimated from 2D TEM images (Figure 5a-c).

From these 3D reconstructions, we also quantified the radial density distribution of Au NCs embedded within PS NPs (Figure 5h). Consistent with our CDFs of the approximate radial depth of Au NCs for many hNPs, 3D tomography showed that the peak density of Au NCs within PS NPs shifted deeper into PS particles with increasing PS-NH₂ content and therefore increasing charge ratio (SI Figure 6). At 10% PS-NH₂, several Au NCs resided on the outside of the PS NP with most just under the surface. TEM tomography also revealed that as the PS-NH₂ content increased to 25% and 50%, a substantial population of Au NCs became internalized to normalized radii less than 0.5. While the PS-NH₂ shell increased in thickness as PS-NH2 content increased, it is also possible that some PS-NH₂ became entrained within the PS core at the highest concentration of 50%. As a result of this potential entrainment, some Au NCs became trapped deep within PS NPs.

Tunable Catalytic Reactions Using Hybrid Nanoparticles. Having explored a wide parameter space to understand the emergence of aggregated, dispersed, and internalized Au NC localization atop and within PS NPs, we tested the ability of hybrid NPs with internalized Au NCs to carry out a catalytic reduction of 4-nitrophenol to 4-aminophenol (Figure 6a). We added equal volumes—and

250

300

350

therefore approximately equal concentrations—of hNPs that are washed and concentrated via centrifugation with PS-NH₂ concentrations of 10%, 25%, and 50% to a reaction mixture containing 0.1 mM 4-nitrophenol and 0.067 M sodium borohydride (NaBH₄).

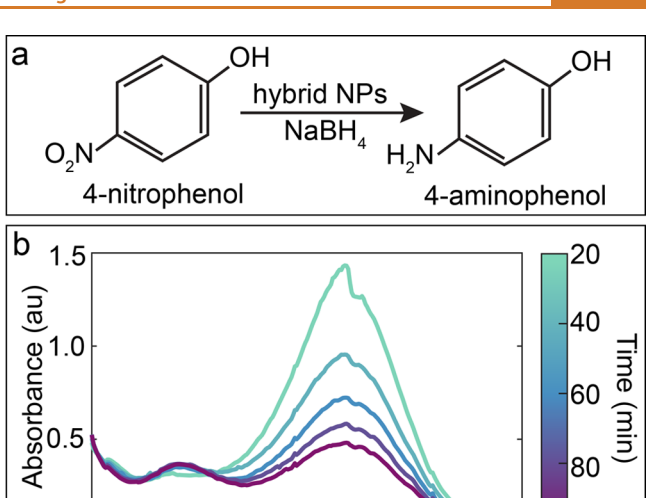
For each PS-NH₂ concentration, we measured UV-Vis absorbance spectra as a function of time over a range of wavelengths, λ , from 250 to 500 nm every 5 min for 2 h. For the reaction that employed 10% PS-NH2 hNPs, we saw a strong peak at the primary absorbance for 4-nitrophenol (λ_{abs} = 405 nm) at time t = 0 min. This peak decreased in magnitude exponentially as a small peak at the primary absorbance for 4aminophenol (λ_{abs} = 294 nm) began to emerge (Figure 6b). We ran additional reduction reactions using 25% and 50% PS-NH₂ hNPs to show the reduction in 4-nitrophenol concentration over time for each hNP formulation (Figure 6c). The reduction of 4-nitrophenol to 4-aminophenol is a first-order reaction, $C(t) = C_0 \exp(-kt)$, where C(t) is the concentration of 4-nitrophenol over time, C_0 is the initial 4nitrophenol concentration, k is the first-order reaction rate constant, and t is time. We obtained rate constants $k = 6 \times 10^{-5}$ 10^{-5} 1/s, 2 × 10^{-5} 1/s, and 7 × 10^{-6} 1/s, for 10%, 25%, and 50% PS-NH₂ hNPs, respectively. These rate constants indicate that reactions using 25% PS-NH, hNPs proceed 3 times slower than those produced using 10% PS-NH₂, while reactions using 50% PS-NH2 hNPs proceed 10 times more slowly. While a small amount of PS-NH2 improved Au NC dispersal atop PS NPs, excess PS-NH2 hindered the rate of reaction. Importantly, the evolution of these reactions reveals that hNPs can be fabricated such that their reaction rates are correlated to the position of Au NCs within hNPs. Additionally, the method of hNP formation presented here may be used to produce materials with varying catalytic properties.

CONCLUSION

Widespread deployment of novel nanomaterials for in situ remediation of groundwater contaminants has long been precluded by their inability to remain stable against aggregation. Additionally, complex fabrication techniques are often required to produce hybrid materials with tunable morphologies and reaction rates. Our work introduces a simple method to fabricate hNPs that relies only on the presence of a good solvent for the polymer to allow for gold nanocatalyst adsorption. Using this method, we showed that increasing incubation time allowed for enhanced aggregation of gold nanocatalysts on polystyrene nanoparticle surfaces, while increasing polymer molecular weight increased their dispersal. We also demonstrated that electrostatic interactions could be used to overcome gold aggregation and promote surface dispersal or internalization of gold nanocatalysts. Since electrostatic interactions only occur between the polymer end-group and nanocatalyst stabilizer, we expect that catalytic reaction rates can be tuned for various citrate-stabilized nanocatalysts, such as platinum or bimetallic nanoparticles, thus making this approach applicable for a wide range of catalytic reduction reactions. Taken together, these results shed light on an approach by which hNPs can be fabricated with tunable morphologies and reveal mechanisms by which catalytic reaction rates can be controlled.

METHODS

Two-Step Hybrid Nanoparticle Fabrication. To prepare polystyrene nanoparticles (PS NPs), we dissolved 0.3 mg/mL un-



400

450

500

80

100

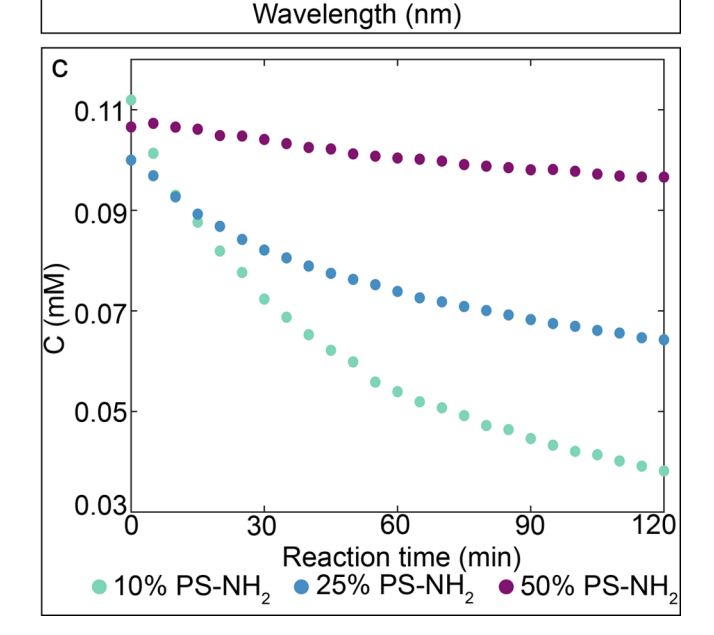


Figure 6. Hybrid nanoparticle morphology controls the reaction rate of a model reduction reaction. (a) Reaction scheme to produce 4-aminophenol from 4-nitrophenol is catalyzed by Au NCs. We add 100 μ L of an hNP suspension to a reaction mixture containing 0.1 mM 4-nitrophenol and 0.067 M NaBH₄. (b) Example UV-vis spectrum of reduction over time using 10% PS-NH₂ hNPs shows a decrease in the magnitude of the primary absorbance of 4-nitrophenol (λ_{abs} = 405 nm) and an increase in that of 4-aminophenol ($\lambda_{abs} = 294$ nm). (c) Plot of concentration (C) measured at $\lambda = 405$ nm every 5 min for 2 h demonstrates that increasing internalization slows reaction rate and efficacy.

cross-linked polystyrene with hydrophobic butyl end-groups of varying molecular weight ($M_n = 10 \text{ kg/mol}$, 99 kg/mol, or 646 kg/ mol, Polymer Source), and therefore a varying number of repeat units ($N \approx 96$, 950, and 6200, respectively) in tetrahydrofuran (Sigma-Aldrich), which is a good solvent for the polymer. We varied surface charge by replacing pure PS with a blend of 0.1 mg/mL PS ($M_n = 10$ kg/mol) and 0.1 mg/mL amine-terminated polystyrene (PS-NH₂, $M_{\rm n}$ = 10 kg/mol, Sigma-Aldrich). We then mixed solutions of varying volume percentages from 0% to 50% PS-NH2 to produce PS/PS-NH₂ colloids. Size measurements obtained from dynamic light scattering (DLS) for all PS and PS/PS-NH2 NPs are reported in Supporting Information (SI) Figures 7 and 8 (Anton Paar Litesizer 500). Zeta potential measurements are also reported in the SI.

Citrate-stabilized gold nanocatalysts (Au NCs) with a diameter, d=5 nm were purchased from Nanopartz. Citrate-stabilized Au NCs with d=20 nm and d=40 nm were synthesized using the method proposed by Turkevich and Frens, ^{52,53} in which we brought a 0.01 wt % solution of chloroauric acid (HAuCl₄) to a rolling boil and then rapidly added a solution of 2 or 0.4 wt % sodium citrate (NaC₆H₅O₇) to produce 20 or 40 nm Au NCs, respectively. The solution continued to boil until a deep red color was achieved after approximately 20 min. Au NCs used in this study had a diameter d=20.9 nm with a PDI of 0.11 or d=38.0 nm with a PDI of 0.26, measured via DLS (SI Figure 9). Au NCs fabricated using this experimental method have been reported to have a zeta potential, $\zeta=-39.7\pm0.7$ mV at pH 9.3. ⁵¹

We performed Flash NanoPrecipitation (FNP) to produce PS or PS/PS-NH₂ NPs using a confined impinging jet (CIJ) mixer (Figure 1a). The prepared PS solutions were impinged against an equal volume of deionized water, which is a poor solvent, or antisolvent, for PS. The effluent stream was then deposited into an antisolvent reservoir to produce NPs with sizes ranging from 200 to 500 nm, depending on the inlet PS concentration. The volume ratio of the polymer solution to the antisolvent stream to the antisolvent reservoir for all experiments was 1:1:1, resulting in a final solvent concentration of 33.3% THF and 66.6% deionized water. We fabricated hNPs by incubating our prepared PS or PS/PS-NH₂ NPs in 33.3% THF with excess Au NCs at a 2:1 ratio with a final solvent composition of 22.2% THF for 1 h (Figure 1a). Any excess, unadsorbed Au NCs were removed from the hNP suspension via centrifugation prior to imaging.

Sample Preparation for Imaging via Transmission Electron Microscopy (TEM). To prepare particles for transmission electron microscopy (TEM), 1.5 mL of hNPs was centrifuged twice to remove any unadsorbed Au NCs (16 000g for 15–45 min, depending on PS NP size) and resuspended in 50–150 μL of deionized water before dropcasting 8 μL of the washed, concentrated suspension onto carbon-coated copper TEM grids (CF-200-Cu, Electron Microscopy Sciences). Samples were left to dry overnight before imaging. All images were acquired using an FEI Talos F200X TEM with an accelerating voltage of 200 kV.

Electron Tomography and Reconstruction of 3D Au NC Distributions. All tomography images were acquired on an FEI Talos F200X TEM with an accelerating voltage of 200 kV at a–1 μ m defocus. Dried, drop cast samples on carbon-coated copper TEM grids were placed onto a $\pm 70^{\circ}$ tomography holder. Images were subsequently taken at 1° increments from -60° to $+60^{\circ}$. Tomographic reconstructions were performed using the ASTRA toolbox in MATLAB. S4 We employed a parallel beam geometry and performed reconstructions with 150 iterations of the simultaneous iterations reconstruction technique.

Image Analysis and Quantification of Hybrid Nanoparticle Morphologies. To quantify Au nanocatalyst adsorption atop the surface of PS NPs, we manually isolated each imaged PS particle for a given data set (i.e., unique experimental conditions and imaging specifications) and binarized using multilevel thresholding in MATLAB. We chose a global threshold level for each data set that allowed for optimal isolation of the contrast obtained only from Au NCs, ignoring any contrast from PS NPs themselves. We then manually adjusted thresholding that did not adequately isolate Au NC contrast for individual particles. To quantify Au NC cluster sizes and count the number of Au NCs adsorbed to each PS NP, we used a built-in MATLAB function, "bwconncomp," and normalized the obtained values by the average Au NC size measured via DLS. Each experimental condition quantified in this paper represents between 40 and 100 individual PS NPs depending on the density of deposited particles on TEM grids.

ASSOCIATED CONTENT

Supporting Information

The Supporting Information is available free of charge at https://pubs.acs.org/doi/10.1021/acsnano.2c04585.

Probability density function of number of adsorbed Au NCs per PS NP when solvent is removed via rotary

evaporation postincubation in Figure S1; quantification of the threshold for considerable Au NC adsorption for 20 and 40 nm Au NCs in Figure S2; average number of adsorbed Au NCs per 100 kg/mol PS NP over increasing incubation times in Figure S3; morphologies of 650 kg/mol hNPs over increasing incubation times in Figure S4; cluster size distributions on the surfaces of 10 kg/mol PS NPs over increasing incubation times in Figure S5; dynamic light scattering (DLS) plots of PS and PS/PS—NH₂ NPs and Au NCs in Figures S6—S8; calculation of charge ratio of NH₂ polymer end-groups to COOH stabilizing groups on Au NCs in Supplementary Calculations, Tables S1 and S2 (PDF)

AUTHOR INFORMATION

Corresponding Author

Rodney D. Priestley — Chemical and Biological Engineering, Princeton University, Princeton, New Jersey 08544, United States; Princeton Institute for the Science and Technology of Materials, Princeton University, Princeton, New Jersey 08544, United States; orcid.org/0000-0001-6765-2933; Email: rpriestl@princeton.edu

Authors

Joanna Schneider — Chemical and Biological Engineering, Princeton University, Princeton, New Jersey 08544, United States; Occid.org/0000-0003-4968-424X

Jason X. Liu – Mechanical and Aerospace Engineering, Princeton University, Princeton, New Jersey 08544, United States

Victoria E. Lee — Chemical and Biological Engineering, Princeton University, Princeton, New Jersey 08544, United States

Robert K. Prud'homme — Chemical and Biological Engineering, Princeton University, Princeton, New Jersey 08544, United States; Occid.org/0000-0003-2858-0097

Sujit S. Datta — Chemical and Biological Engineering, Princeton University, Princeton, New Jersey 08544, United States; Occid.org/0000-0003-2400-1561

Complete contact information is available at: https://pubs.acs.org/10.1021/acsnano.2c04585

Notes

The authors declare no competing financial interest.

ACKNOWLEDGMENTS

The authors thank R. Bay, C. Browne, and D. Scott for helpful feedback on the manuscript, as well as N. Bizmark, A. Hancock, S. Maguire, A. McGaughey, J. Ott, and J. Schreiber for stimulating discussions. This work was supported by the National Science Foundation (NSF) Materials Research Science and Engineering Center (MRSEC; DMR-2011750), as well as funding from the New Jersey Water Resources Research Institute (to S.S.D.) and a Mary and Randall Hack Graduate Award of the High Meadows Environmental Institute (to J.S.). The authors also acknowledge the use of Princeton's Imaging and Analysis Center (IAC), which is partially supported by the Princeton Center for Complex Materials (PCCM), a National Science Foundation (NSF) Materials Research Science and Engineering Center (MRSEC; DMR-2011750).

REFERENCES

- (1) Balazs, A. C.; Emrick, T.; Russell, T. P. Nanoparticle Polymer Composites: Where Two Small Worlds Meet. *Science* **2006**, *314*, 1107–1110.
- (2) Van Schooneveld, M. M.; Gloter, A.; Stephan, O.; Zagonel, L. F.; Koole, R.; Meijerink, A.; Mulder, W. J.; De Groot, F. M. Imaging and Quantifying the Morphology of an Organic–Inorganic Nanoparticle at the Sub-Nanometre Level. *Nat. Nanotechnol.* **2010**, *5*, 538–544.
- (3) Li, S.; Meng Lin, M.; Toprak, M. S.; Kim, D. K.; Muhammed, M. Nanocomposites of Polymer and Inorganic Nanoparticles for Optical and Magnetic Applications. *Nano Rev.* **2010**, *1*, 5214.
- (4) Mai, Y.; Eisenberg, A. Selective Localization of Preformed Nanoparticles in Morphologically Controllable Block Copolymer Aggregates in Solution. *Acc. Chem. Res.* **2012**, *45*, 1657–1666.
- (5) Yi, Y.; Sanchez, L.; Gao, Y.; Yu, Y. Janus Particles for Biological Imaging and Sensing. *Analyst* **2016**, *141*, 3526–3539.
- (6) Lim, C. W.; Lee, I. S. Magnetically Recyclable Nanocatalyst Systems for the Organic Reactions. *Nano Today* **2010**, *5*, 412–434.
- (7) Gijs, M. A.; Lacharme, F.; Lehmann, U. Microfluidic Applications of Magnetic Particles for Biological Analysis and Catalysis. *Chem. Rev.* **2010**, *110*, 1518–1563.
- (8) Zhu, Y.; Fan, L.; Yang, B.; Du, J. Multifunctional Homopolymer Vesicles for Facile Immobilization of Gold Nanoparticles and Effective Water Remediation. *ACS Nano* **2014**, *8*, 5022–5031.
- (9) Gross, E.; Toste, F. D.; Somorjai, G. A. Polymer-Encapsulated Metallic Nanoparticles as a Bridge Between Homogeneous and Heterogeneous Catalysis. *Catal. Lett.* **2015**, *145*, 126–138.
- (10) Li, L.; Fan, M.; Brown, R. C.; Van Leeuwen, J.; Wang, J.; Wang, W.; Song, Y.; Zhang, P. Synthesis, Properties, and Environmental Applications of Nanoscale Iron-Based Materials: A Review. *Crit. Rev. Environ. Sci. Technol.* **2006**, 36, 405–431.
- (11) Li, X.-q.; Elliott, D. W.; Zhang, W.-x. Zero-Valent Iron Nanoparticles for Abatement of Environmental Pollutants: Materials and Engineering Aspects. *Crit. Rev. Solid State Mater. Sci.* **2006**, *31*, 111–122.
- (12) Pacheco, S.; Medina, M.; Valencia, F.; Tapia, J. Removal of Inorganic Mercury from Polluted Water Using Structured Nanoparticles. J. Environ. Eng. Div. (Am. Soc. Civ. Eng.) 2006, 132, 342—349.
- (13) Hristovski, K.; Baumgardner, A.; Westerhoff, P. Selecting Metal Oxide Nanomaterials for Arsenic Removal in Fixed Bed Columns: from Nanopowders to Aggregated Nanoparticle Media. *J. Hazard. Mater.* **2007**, *147*, 265–274.
- (14) Phenrat, T.; Saleh, N.; Sirk, K.; Tilton, R. D.; Lowry, G. V. Aggregation and Sedimentation of Aqueous Nanoscale Zero-Valent Iron Dispersions. *Environ. Sci. Technol.* **2007**, *41*, 284–290.
- (15) Keller, A. A.; Wang, H.; Zhou, D.; Lenihan, H. S.; Cherr, G.; Cardinale, B. J.; Miller, R.; Ji, Z. Stability and Aggregation of Metal Oxide Nanoparticles in Natural Aqueous Matrices. *Environ. Sci. Technol.* **2010**, *44*, 1962–1967.
- (16) Lin, Y.; Qiao, Y.; Wang, Y.; Yan, Y.; Huang, J. Self-Assembled Laminated Nanoribbon-Directed Synthesis of Noble Metallic Nanoparticle-Decorated Silica Nanotubes and Their Catalytic Applications. *J. Mater. Chem.* **2012**, 22, 18314–18320.
- (17) Lu, F.; Astruc, D. Nanocatalysts and Other Nanomaterials for Water Remediation from Organic Pollutants. *Coord. Chem. Rev.* **2020**, 408. 213180.
- (18) Tiraferri, A.; Chen, K. L.; Sethi, R.; Elimelech, M. Reduced Aggregation and Sedimentation of Zero-Valent Iron Nanoparticles in the Presence of Guar Gum. *J. Colloid Interface Sci.* **2008**, 324, 71–79.
- (19) Phenrat, T.; Fagerlund, F.; Illangasekare, T.; Lowry, G. V.; Tilton, R. D. Polymer-Modified Fe⁰ Nanoparticles Target Entrapped NAPL in Two Dimensional Porous Media: Effect of Particle Concentration, NAPL Saturation, and Injection Strategy. *Environ. Sci. Technol.* **2011**, *45*, 6102–6109.
- (20) Xiang, A.; Yan, W.; Koel, B. E.; Jaffé, P. R. Poly(Acrylic Acid) Coating Induced 2-Line Ferrihydrite Nanoparticle Transport in Saturated Porous Media. *J. Nanopart. Res.* **2013**, *15*, 1705.

- (21) Yan, W.; Lien, H.-L.; Koel, B. E.; Zhang, W. Iron Nanoparticles for Environmental Clean-Up: Recent Developments and Future Outlook. *Environ. Sci. Process Impacts* **2013**, *15*, 63–77.
- (22) Xiang, A.; Zhou, S.; Koel, B. E.; Jaffé, P. R. Transport of Poly(Acrylic Acid) Coated 2-Line Ferrihydrite Nanoparticles in Saturated Aquifer Sediments for Environmental Remediation. *J. Nanopart. Res.* **2014**, *16*, 2294.
- (23) Yang, S.-M.; Kim, S.-H.; Lim, J.-M.; Yi, G.-R. Synthesis and Assembly of Structured Colloidal Particles. *J. Mater. Chem.* **2008**, *18*, 2177–2190.
- (24) Ianiro, A.; Wu, H.; van Rijt, M. M.; Vena, M. P.; Keizer, A. D.; Esteves, A.; Tuinier, R.; Friedrich, H.; Sommerdijk, N. A.; Patterson, J. P. Liquid–Liquid Phase Separation During Amphiphilic Self-Assembly. *Nature Chem.* **2019**, *11*, 320–328.
- (25) Wong, C. K.; Qiang, X.; Müller, A. H.; Gröschel, A. H. Self-Assembly of Block Copolymers into Internally Ordered Microparticles. *Prog. Polym. Sci.* **2020**, *102*, 101211.
- (26) Higuchi, T.; Tajima, A.; Yabu, H.; Shimomura, M. Spontaneous Formation of Polymer Nanoparticles with Inner Micro-Phase Separation Structures. *Soft Matter* **2008**, *4*, 1302–1305.
- (27) Huh, J.; Jung, J. Y.; Lee, J. U.; Cho, H.; Park, S.; Park, C.; Jo, W. H. Supramolecular Assembly of End-Functionalized Polymer Mixtures Confined in Nanospheres. ACS Nano 2011, 5, 115–122.
- (28) Yabu, H. Self-Organized Precipitation: an Emerging Method for Preparation of Unique Polymer Particles. *Polym. J.* **2013**, *45*, 261–268
- (29) Yabu, H. Fabrication of Nanostructured Composite Microspheres Based on the Self-Assembly of Polymers and Functional Nanomaterials. *Part. Part. Syst. Charact.* **2019**, *36*, 1900178.
- (30) Lee, V. E.; Sosa, C.; Liu, R.; Prud'homme, R. K.; Priestley, R. D. Scalable Platform for Structured and Hybrid Soft Nanocolloids by Continuous Precipitation in a Confined Environment. *Langmuir* **2017**, 33, 3444–3449.
- (31) Sosa, C.; Lee, V. E.; Grundy, L. S.; Burroughs, M. J.; Liu, R.; Prud'homme, R. K.; Priestley, R. D. Combining Precipitation and Vitrification to Control the Number of Surface Patches on Polymer Nanocolloids. *Langmuir* **2017**, *33*, 5835–5842.
- (32) Grundy, L. S.; Lee, V. E.; Li, N.; Sosa, C.; Mulhearn, W. D.; Liu, R.; Register, R. A.; Nikoubashman, A.; Prud'homme, R. K.; Panagiotopoulos, A. Z.; et al. Rapid Production of Internally Structured Colloids by Flash Nanoprecipitation of Block Copolymer Blends. ACS Nano 2018, 12, 4660–4668.
- (33) Kao, J.; Thorkelsson, K.; Bai, P.; Rancatore, B. J.; Xu, T. Toward Functional Nanocomposites: Taking the Best of Nanoparticles, Polymers, and Small Molecules. *Chem. Soc. Rev.* **2013**, *42*, 2654–2678.
- (34) Gao, D.; Liu, N.; Li, W.; Han, Y. Fabrication of Nanoporous Polymeric Crystalline ${\rm TiO_2}$ Composite for Photocatalytic Degradation of Aqueous Organic Pollutants Under Visible Light Irradiation. *Appl. Organomet. Chem.* **2018**, 32, No. e4119.
- (35) Duarah, R.; Karak, N. Hyperbranched Polyurethane/Reduced Carbon Dot-Zinc Oxide Nanocomposite-Mediated Solar-Assisted Photocatalytic Degradation of Organic Contaminant: An Approach Towards Environmental Remediation. *Chem. Eng. J.* **2019**, *370*, 716–728
- (36) Zeng, J.; Peng, C.; Wang, X.; Wang, R.; Zhang, N.; Xiong, S. One-Pot Self-Assembled TiO₂/Graphene/Poly (Acrylamide) Superporous Hybrid for Photocatalytic Degradation of Organic Pollutants. *J. Appl. Polym. Sci.* **2019**, *136*, 47033.
- (37) Shenhar, R.; Norsten, T. B.; Rotello, V. M. Polymer-Mediated Nanoparticle Assembly: Structural Control and Applications. *Adv. Mater.* **2005**, *17*, 657–669.
- (38) Tian, J.; Jin, J.; Zheng, F.; Zhao, H. Self-Assembly of Gold Nanoparticles and Polystyrene: A Highly Versatile Approach to the Preparation of Colloidal Particles with Polystyrene Cores and Gold Nanoparticle Coronae. *Langmuir* **2010**, *26*, 8762–8768.
- (39) Gao, C.; Lyu, F.; Yin, Y. Encapsulated Metal Nanoparticles for Catalysis. Chem. Rev. 2021, 121, 834–881.

- (40) Yabu, H.; Koike, K.; Motoyoshi, K.; Higuchi, T.; Shimomura, M. Preparation of Core–Shell Organic–Inorganic Nanocomposite Particles Based on Phase Separation of a Polymer Blend. *Chem. Lett.* **2009**, *38*, 964–965.
- (41) Yabu, H.; Koike, K.; Motoyoshi, K.; Higuchi, T.; Shimomura, M. A Novel Route for Fabricating Metal-Polymer Composite Nanoparticles with Phase-Separated Structures. *Macromol. Rapid Commun.* **2010**, *31*, 1267–1271.
- (42) Yabu, H.; Jinno, T.; Koike, K.; Higuchi, T.; Shimomura, M. Nanoparticle Arrangements in Block Copolymer Particles with Microphase-Separated Structures. *J. Polym. Sci. B Polym. Phys.* **2011**, 49, 1717–1722.
- (43) Kumar, V.; Prud'homme, R. K. Nanoparticle Stability: Processing Pathways for Solvent Removal. *Chem. Eng. Sci.* **2009**, *64*, 1358–1361.
- (44) Tao, J.; Chow, S. F.; Zheng, Y. Application of Flash NanoPrecipitation to Fabricate Poorly water-Soluble Drug Nanoparticles. *Acta Pharm. Sin. B* **2019**, *9*, 4–18.
- (45) Nikoubashman, A.; Lee, V. E.; Sosa, C.; Prud'homme, R. K.; Priestley, R. D.; Panagiotopoulos, A. Z. Directed Assembly of Soft Colloids Through Rapid Solvent Exchange. *ACS Nano* **2016**, *10*, 1425–1433.
- (46) Pagels, R. F.; Edelstein, J.; Tang, C.; Prud'homme, R. K. Controlling and Predicting Nanoparticle Formation by Block Copolymer Directed Rapid Precipitations. *Nano Lett.* **2018**, *18*, 1139–1144.
- (47) Liu, J. X.; Bizmark, N.; Scott, D. M.; Register, R. A.; Haataja, M. P.; Datta, S. S.; Arnold, C. B.; Priestley, R. D. Evolution of Polymer Colloid Structure During Precipitation and Phase Separation. *JACS Au* **2021**, *1*, 936–944.
- (48) Rubinstein, M.; Colby, R. H., et al. *Polymer Physics*; Oxford University Press: New York, 2003; Vol. 23.
- (49) Lu, H. D.; Rummaneethorn, P.; Ristroph, K. D.; Prud'homme, R. K. Hydrophobic Ion Pairing of Peptide Antibiotics for Processing into Controlled Release Nanocarrier Formulations. *Mol. Pharmaceutics* **2018**, *15*, 216–225.
- (50) Ristroph, K. D.; Prud'homme, R. K. Hydrophobic Ion Pairing: Encapsulating Small Molecules, Peptides, and Proteins into Nanocarriers. *Nanoscale Adv.* **2019**, *1*, 4207–4237.
- (51) Ivanov, M. R.; Bednar, H. R.; Haes, A. J. Investigations of the Mechanism of Gold Nanoparticle Stability and Surface Functionalization in Capillary Electrophoresis. *ACS Nano* **2009**, *3*, 386–394.
- (52) Turkevich, J.; Stevenson, P. C.; Hillier, J. A Study of the Nucleation and Growth Processes in the Synthesis of Colloidal Gold. *Discuss. Faraday Soc.* **1951**, *11*, 55–75.
- (53) Frens, G. Controlled Nucleation for the rRegulation of the Particle Size in Monodisperse Gold Suspensions. *Nature Phys. Sci.* **1973**, 241, 20–22.
- (54) Van Aarle, W.; Palenstijn, W. J.; De Beenhouwer, J.; Altantzis, T.; Bals, S.; Batenburg, K. J.; Sijbers, J. The ASTRA Toolbox: A Platform for Advanced Algorithm Development in Electron Tomography. *Ultramicroscopy* **2015**, *157*, 35–47.

□ Recommended by ACS

Centrifugation-Assisted Growth of Single-Crystalline Grains in Microcapsules

Young Geon Kim, Shin-Hyun Kim, et al.

JANUARY 17, 2023

ACS NANO

READ 🗹

Flask-like Janus Colloidal Motors with Explicit Direction and Tunable Speed

Yingchun Long, Fuxin Liang, et al.

OCTOBER 17, 2022

ACS NANO

READ 🗹

Directed Assembly of Nanomaterials for Making Nanoscale Devices and Structures: Mechanisms and Applications

Zhimin Chai, Ahmed A. Busnaina, et al.

OCTOBER 21, 2022

ACS NANO

READ 🗹

Influence of Polymer Characteristics on the Self-Assembly of Polymer-Grafted Metal-Organic Framework Particles

Kyle Barcus, Seth M. Cohen, et al.

OCTOBER 17, 2022

ACS NANO

READ **C**

Get More Suggestions >